Quantifying slab sinking rates using global geodynamic models with data-assimilation

Diandian Peng[*], Lijun Liu

University of Illinois at Urbana-Champaign, Urbana, IL, 61801, USA

A B S T R A C T

Recent tomography-based tectonic (tomotectonic) reconstructions provide important new insights on past subduction processes. However, some of these exercises violate key geological observations. We suggest this is due to two common simplifications: 1) slabs sink vertically after subduction with their present geographic locations marking past trenches, and 2) slabs sink at a constant rate throughout the mantle with their present mantle depths linearly correlating with their subduction ages. In this study, we investigate the 4D evolution of subducted slabs using global data-assimilation models that successfully reproduce observed mantle slabs along all major subduction zones. We find that slabs can migrate laterally up to 6000 km while descending toward the core-mantle boundary (CMB). This enormous displacement mostly reflects strong and geographically variable horizontal mantle flow. The model results further show that the vertical sinking rate of slabs varies with subduction duration, depth, and geographic locations. The slab sinking rate generally decreases with increasing depth, ranging from >2 cm/yr above 1600 km depth to zero at ~500 km above the CMB. The sinking rate locally peaks at the asthenospheric and mid-mantle depths and diminishes at the base of the transition zone. We further find that surface plate motion strongly affects the horizontal migration of slabs but less affects their sinking rate. These results suggest cautions on inferring past tectonic events based on seismic tomography.

1. Introduction

Seismic tomography provides key constraints for the evolution of subducted slabs inside the mantle. The spatial distribution of the seismically imaged slabs are widely used to infer the properties of past subduction and resulting surface geology (Bunge and Grand, 2000; Butterworth et al., 2014; Grand et al., 1997; Liu et al., 2008; Replumaz et al., 2010; Sigloch and Mihalynuk, 2013; van der Meer et al., 2010; Wu et al., 2016; Wu and Suppe, 2018). An important application focuses on the location and evolution of past subduction zones based on the present-day mantle seismic images. This tomotectonic reconstruction has been implemented at both global (Butterworth et al., 2014; van der Meer et al., 2018; van der Meer et al., 2010) and regional scales (Clennett et al., 2020; Domeier et al., 2017; Replumaz et al., 2010; Schellart et al., 2009; Sigloch and Mihalynuk, 2013).

In previous studies, the slabs are often thought to sink almost vertically in the mantle with limited lateral motion (Butterworth et al., 2014; Replumaz et al., 2010; Replumaz et al., 2004; Sigloch and Mihalynuk, 2013; van der Meer et al., 2010). The geographic locations

of imaged slabs are considered those of past subduction zones, while surface geology records are utilized to estimate the subduction age of these slabs. Due to uncertainties of both the seismic image and geologic events, another key input is the slab vertical sinking rate, which has been commonly approximated in two approaches. The first one either assumes or infers that a slab sinks through the mantle at a nearly constant rate, so that the average sinking rate is the slope of the current depth of the slab and the geologically inferred age of past subduction (Butterworth et al., 2014; Sigloch and Mihalynuk, 2013; van der Meer et al., 2010). The second approach locates the depth range of a piece of slab and the time range of the corresponding geological event, to determine both the global average and in situ sinking rates (van der Meer et al., 2018). Thus, generated slab sinking rates vary greatly among different studies, with their values ranging from as small as 1 cm/yr (e.g., Sigloch and Mihalynuk, 2013; van der Meer et al., 2010) to as large as 2 cm/yr (e.g., Domeier et al., 2017).

While these recent tomotectonic reconstructions have contributed significantly to our understanding of past subduction and geology, they also raise major controversies on these topics (Liu, 2014; Pavlis et al.,

---

2019). We suggest that a key reason lies in the poorly constrained slab sinking rate. This is because, first, the sinking rate of a certain slab could be time dependent. For example, before the slab reaches the lower mantle, its sinking rate could be large due to the weak ambient upper mantle. After the slab encounters the 660 km discontinuity, both the plausible viscosity increases, and the negative Clapeyron Slope could slow down slab sinking rate. When the slab is finally approaching the core-mantle boundary (CMB), the sinking rate should decrease further to eventually vanish since the CMB represents a non-penetrable boundary for slabs. Second, inferring slab sinking rates from their depth-age relationship could be inaccurate. On one hand, seismic studies suggest that slabs have different dip angles at various depths of the mantle, suggesting that they do not always sink vertically (Fukao and Obayashi, 2013; Hayes et al., 2018). In the case when a slab with an overall flat geometry sinks through the mantle, its depth-age slope would imply a sinking rate too slow to be true. On the other hand, the depth-age relationship may also have large age uncertainties on the involved geological events, such as the uncertainty for the terrane accretion history along western North America (Pavlis et al., 2019). Finally, numerous geodynamic simulations have shown that slabs could migrate laterally a long distance within the mid-mantle after subduction (Liu et al., 2021a; Ma et al., 2019; Mao and Zhong, 2018; Peng et al., 2021b; Peng et al., 2021a). In these cases, presuming a vertical slab trajectory would lead to apparently erroneous trench locations during the past, thus misinterpretation of the geological records.

In this study, we attempt an assessment of the sinking history of slabs through global numerical simulations based on data assimilation. By satisfying both the subduction history and present mantle structures, these models provide a quantitative numerical framework where the 4-D migration of mantle slabs could be recorded and analyzed. The presented evolutionary models not only reproduced the major slabs seen in tomography today, but also match several key ancient abnormal subduction episodes like the flat Izanagi and Farallon subduction events during the latest Cretaceous (Liu et al., 2021b; Peng et al., 2021b). Based on these model results, we analyze the history and amounts of horizontal vs vertical migration of slabs during the past 200 Myr. We present a statistical analysis about the sinking rate of slabs on a global scale as well as along individual subduction zones.

2. Method and model setup

To properly reproduce the subduction history since early Mesozoic, we perform global thermal-chemical models with data assimilation (Hu et al., 2018; Liu and Stegman, 2011; Peng et al., 2021a, 2021b) from 200 Ma. We assume an incompressible mantle that satisfies the Boussinesq approximation, and carry out the simulations using the spherical mantle code CitcomS (McNamara and Zhong, 2004; Tan et al., 2006; Zhong et al., 2008) which solves the following equations for the conservation of mass, momentum and energy, as well as the advection of chemical particles:

$$\nabla \cdot \overrightarrow{u} = 0 \tag{1}$$

$$-\nabla P + \nabla \cdot \left[\eta \left(\nabla \overrightarrow{u} + \nabla^{T} \overrightarrow{u}\right)\right] + (\rho_{m}\alpha\Delta T + \Delta\rho_{c})\overrightarrow{g} = 0 \tag{2}$$

$$\frac{\partial T}{\partial t} + \overrightarrow{u} \cdot \nabla T = \kappa \nabla^{2} T \tag{3}$$

$$\frac{\partial C}{\partial t} + \overrightarrow{u} \cdot \nabla C = 0 \tag{4}$$

where $\overrightarrow{u}$ is the velocity, P is dynamic pressure, η is dynamic viscosity, ρ_{m} is the density of the ambient mantle, α is thermal expansion coefficient, ΔT is temperature anomaly, $\Delta\rho_{c}$ is compositional density anomaly, $\overrightarrow{g}$ is gravitational acceleration, and C is composition.

The global mantle domain is discretized into a high-resolution finite-element mesh with 12 spherical caps, each having $257 \times 257 \times 113$ nodes in latitude×longitude×radius dimensions. The resolution in the horizontal direction is ~23 km at the surface and ~12 km at the core-mantle boundary (CMB), and that in the vertical direction is ~12 km near the surface, ~26 km near the CMB, and ~31 km in the mid-mantle. The base of the mantle is free slip while the surface assimilates velocities from a recent plate reconstructions (Müller et al., 2016). The temperature profile for oceanic plates follows a plate model with seafloor age adopted from the plate reconstruction (Müller et al., 2016), while the continents have a steady-state initial temperature profile (Fig. S1a). The viscosity structure depends on depth, temperature, and composition, with a layered background viscosity profile and a reference viscosity of 10^{21} Pas (Fig. S1b). A total of ~1.8 billion tracers with thirteen compositional flavors are used to track the deformation and migration of different chemical compositions. More details about the model setup and parameters can be found in Peng et al. (2021a, 2021b).

To track the evolution of slabs through the mantle, we assign some additional tracer properties in addition to those tracking location and compositions. Upon subduction, each composition tracer within the downgoing slab is assigned a unique ID. This ID marks the individual subduction zone along which the tracer subducts. We consider several major subduction zones, including northwestern Pacific, southwestern Pacific, southeastern Pacific, southern Pacific, northern Pacific, northeastern Pacific, Mongol-Okhotsk and Tethyan subduction zones. For each tracer within the interior (20–40 km below the surface) of the oceanic plate, we further record its corresponding seafloor age. When this tracer approaches the subduction zone (within 100 km from the trench), we record the geological time (i.e., the time of subduction). In addition, each tracer carries basic information like position (longitude, latitude, and depth) and velocity components (at three directions). These recorded properties for oceanic slabs will be used later for the analyses of slab migration and velocities.

3. Quantitative analysis of model results

A premise of this study is that the presented geodynamic models properly reproduce the past evolution of major slabs within the mantle. Although a model can never be claimed as fully representing the reality, a promising way for evaluating a model is to test key model features against observations. This is first encouraged by the improved constraints in plate reconstructions (e.g., Müller et al., 2016) that enters the model as boundary conditions and the well calibrated physical principals of mantle convection (e.g., Zhong et al., 2008) that allows a reasonable thermal-mechanical connection with the evolving slabs and surface tectonics. Consequently, the model evaluation effort could focus on the effects of the still-uncertain mantle dynamic properties like its viscosity structure.

For a given surface kinematic history, mantle viscosity mostly affects the evolving geometry of slabs over time, which could be assessed through hindcasting past geological events and reproducing present mantle seismic structures. In two recent studies, we showed that the global models with data-assimilation properly generate the flat subduction of the Izanagi slab and the Farallon slab during the latest Cretaceous (Peng et al., 2021b) as well as the stagnant East Asian slabs at the present-day (Peng et al., 2021a). In this study, we present the results from two of these recent models. Model 1 is the reference case in Peng et al. (2021a, 2021b), and Model 2 (the Model 4 in Peng et al., 2021a) has a stronger lower mantle than in Model 1 (Fig. S1b).

To evaluate these model results, we first compare them to the tomography images in map view (Fig. 1). At 2600 km depth, the most prominent features in tomography (e.g., Fig. 1a) are the Pacific and African Large Low Shear Velocity Provinces (LLSVPs). Both Model 1 and Model 2 predict prominent high temperature anomalies in these regions (Fig. 1b-c), with similar locations and geometry to those of the observed LLSVPs in SEMUCB-WM1 (French and Romanowicz, 2014). Locally, the structure beneath North Pacific is not well predicted, with the modeled
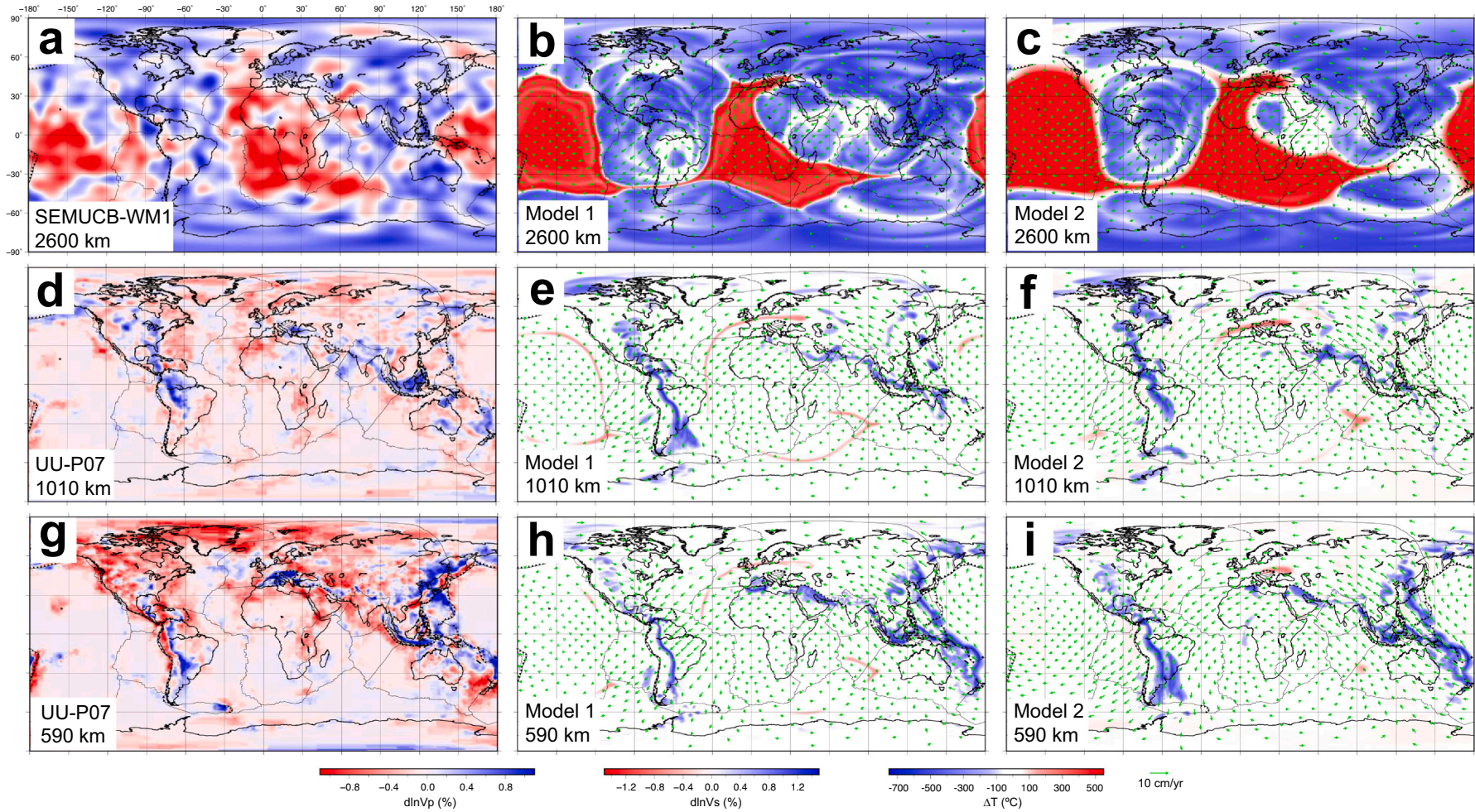
Fig. 1. Comparison of model results with tomography in map views. (a) S-wave velocities anomalies at 2600 km in SEMUCB-WM1. (b,c) Simulated temperature and velocity (green arrows) at 2600 km in Model 1 and Model 2, respectively. (d) P-wave velocities anomalies at 1010 km in UU-P07. (e,f) The same as (b,c) but at 1010 km depth. (g) P wave velocities anomalies at 590 km in UU-P07. (h,i) The same as (b,c) but at 590 km depth. (For interpretation of the references to colour in this figure legend, the reader is referred to the web version of this article.)

LLSVP being further north. The mismatch could reflect the lack of the recently interocean subduction in the region (Clennett et al., 2020; Domeier et al., 2017) in our simulation. At mid-mantle (1010 km) and mantle transition zone (MTZ) depths, the major features in the tomography model UU-P07 (Amaru, 2007) are slabs beneath Americas, Eurasia and Tonga, which are well reproduced in both models (Fig. 1d-i). With a closer examination, slabs in Model 1 at these depths are slightly thinner than those in Model 2, consistent with the higher lower-mantle viscosity, thus slab thickening, in the latter.

Next, we compare the modeled slabs with tomography along the four major subduction zones in existence since the Mesozoic (Fig. 2). Beneath East Asia, both Model 1 and Model 2 predict the prominent stagnant slab, with additional tomographic images shown in Peng et al. (2021a). Below South Asia across the Tethyan convergent boundary, both models fit the tomography result, while Model 1 has slightly deeper slabs than Model 2 due to a weaker lower mantle. Here, Model 1 fits tomography slightly better than Model 2. In North America where the Farallon plate subducted, the slabs in Model 1 are westward shifted or at greater depths relative to those in Model 2, which better match tomography. Along the cross section through South America, Model 2 predicts the seismically imaged stagnant Nazca slab, but that in Model 1 penetrates deep into the lower mantle. Collectively, slabs in Model 2 match tomography better than in Model 1.

Besides the above qualitative comparison (Figs. 1, 2), we also perform a more quantitative evaluation of the model results by examining the match in the spherical hormonic domain following previous studies (Becker and Boschi, 2002; Mao and Zhong, 2019). Here we compare model results with two S wave tomography images. We first convert the modeled temperature anomalies to density anomalies following $\delta\rho/\rho = -\alpha\delta T$, where δT is the temperature deviation from the global horizontal average at a certain depth. Next, these density anomalies are scaled to S wave anomalies following a scaling factor $\Lambda = dlnv_s/dln\rho$, whose value is 3.6 (Becker and Boschi, 2002; Mao and Zhong, 2019). Then, at a given mantle depth from 50 to 2815 km, we decompose both the modeled and observed seismic anomalies (interpolated to

each model depth) into spherical harmonics up to degree 20. With the coefficients for degree l and order m being $\{a_{lm}, b_{lm}\}$ for modeled and $\{c_{lm}, d_{lm}\}$ for observed seismic anomalies, the correlation r^l between the two fields at degree l follows

$$r^l = \frac{\sum_{m=0}^{l}(a_{lm}c_{lm} + b_{lm}d_{lm})}{\sqrt{\sum_{m=0}^{l}(a_{lm}^2 + b_{lm}^2)}\sqrt{\sum_{m=0}^{l}(c_{lm}^2 + d_{lm}^2)}} \quad (5)$$

The total correlation from degree 1 to degree l_{max} is

$$r_{l_{max}}^{tot} = \frac{\sum_{l=1}^{l_{max}}\sum_{m=0}^{l}(a_{lm}c_{lm} + b_{lm}d_{lm})}{\sqrt{\sum_{l=1}^{l_{max}}\sum_{m=0}^{l}(a_{lm}^2 + b_{lm}^2)}\sqrt{\sum_{l=1}^{l_{max}}\sum_{m=0}^{l}(c_{lm}^2 + d_{lm}^2)}} \quad (6)$$

The weighted average correlation over all M depth layers (z_j, j from 1 to M) between 50 km and 2815 km is

$$\langle r_{l_{max}} \rangle = \frac{\sum_{j=1}^{M}w_j r_{l_{max}}^{tot}(z_j)}{\sum_{i=1}^{M}w_j} \quad (7)$$

where $w_j = h_j(R - z_j)^2$ is the weight of layer j. R is the Earth's radius and h_j is the thickness of the layer.

The weighted-average correlation coefficient between Model 1 and SEMUCB-WM1 (French and Romanowicz, 2014) over the whole mantle is $\langle r_8 \rangle = 0.52$ and $< r_{20} > = 0.37$ for degrees 1–8 and 1–20, respectively (Fig. 3). When the comparison is limited to the lower mantle, the correlation coefficients are $\langle r_8 \rangle = 0.55$ and $< r_{20} > = 0.37$. When comparing Model 1 with tomography S40RTS (Ritsema et al., 2011), the results are even better, with $\langle r_8 \rangle = 0.53$ and $< r_{20} > = 0.39$ in the depth range of 50–2815 km, and $< r_8 > = 0.56$ and $< r_{20} > = 0.38$ in the lower mantle (Fig. 3). The whole-mantle weighted average correlation coefficients between Model 2 and SEMUCB-WM1 are $< r_8 > = 0.49$ and $< r_{20} > = 0.36$, while those between Model 2 and S40RTS are $< r_8 > =$
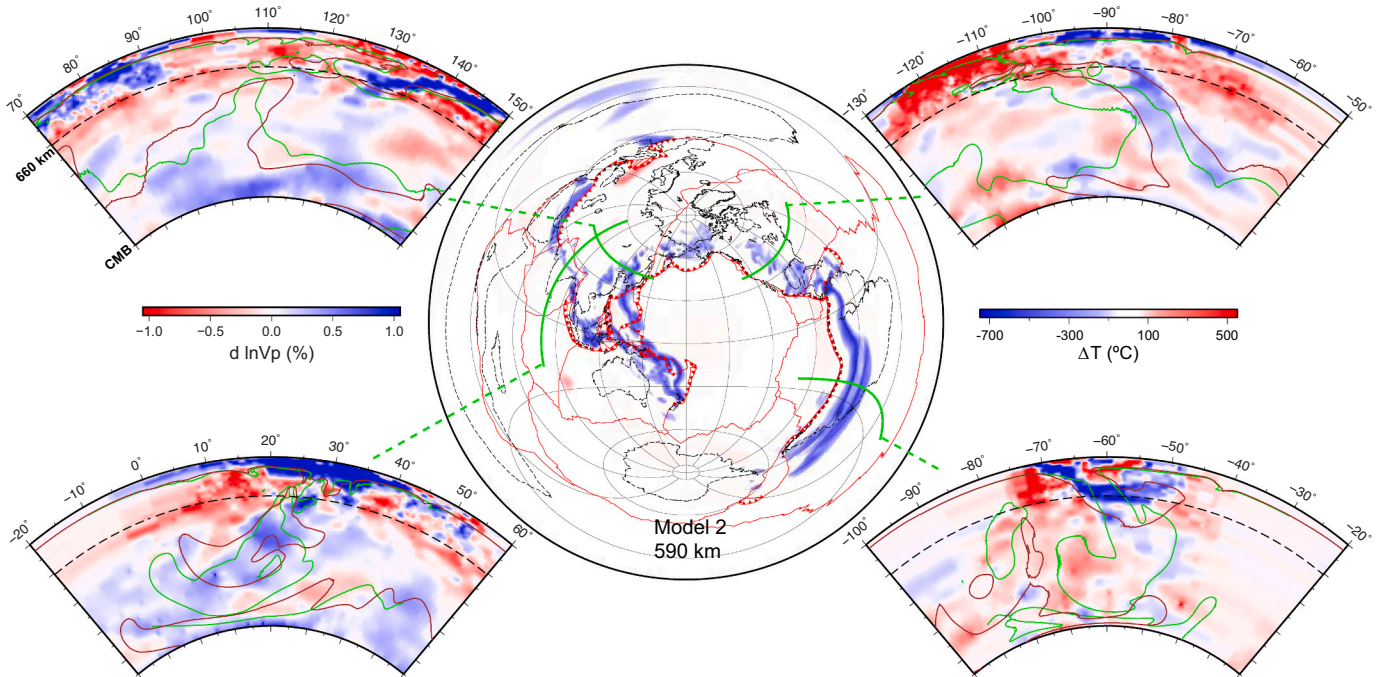
Fig. 2. Comparison of model results with tomography along different cross sections. The panel in the center shows the simulated present mantle temperature at 590 km from Model 2. The background colour shows the P wave velocity anomalies in UU-P07 along four major subduction zones, including East Asia, South Asia, North America, and South America. The colour contour in the cross sections shows modeled low temperature anomalies (100 °C colder than ambient), with Model 1 marked in green and Model 2 in magenta. (For interpretation of the references to colour in this figure legend, the reader is referred to the web version of this article.)
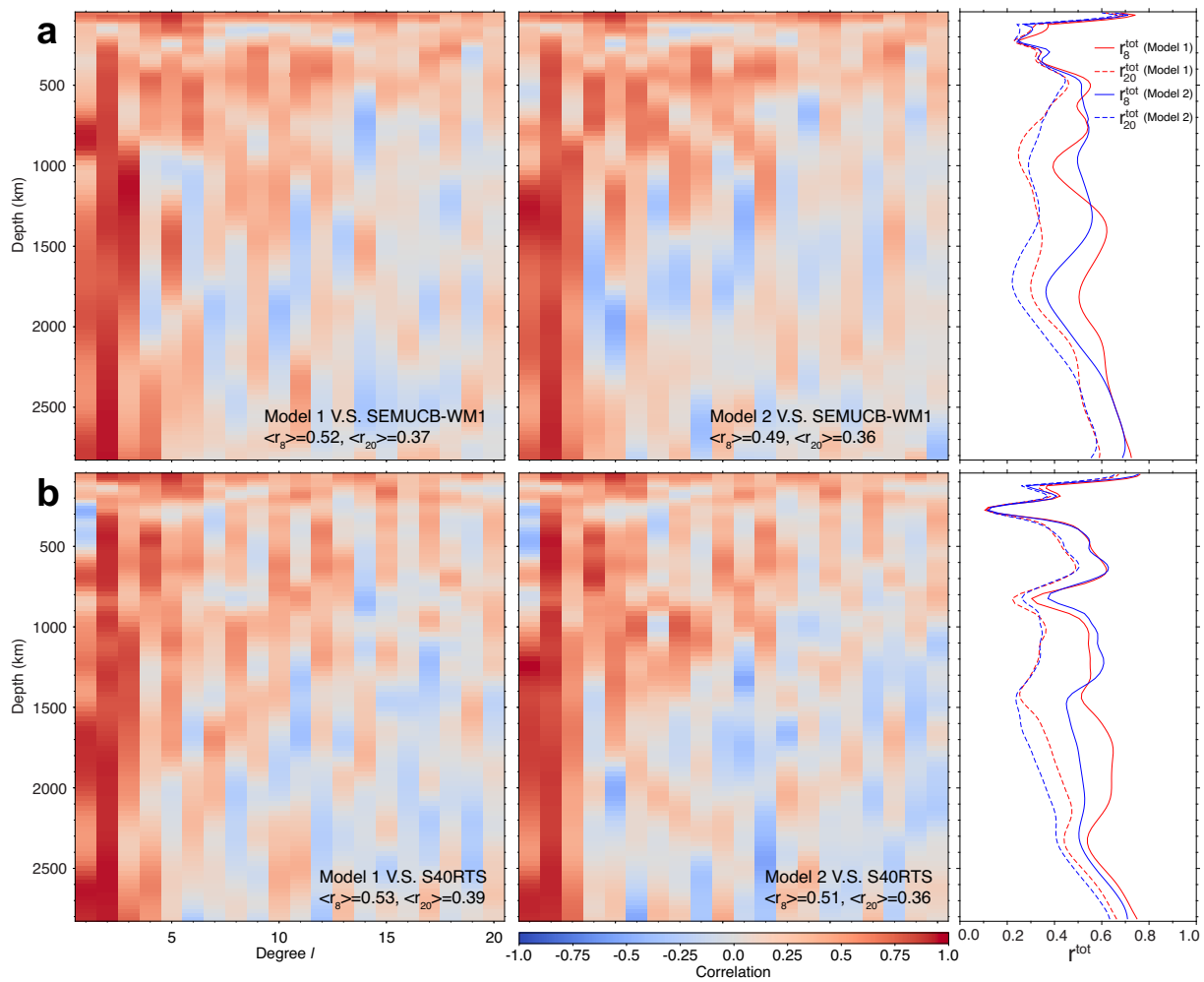
Fig. 3. The correlations between models and S wave tomography models up to spherical harmonic degree 20 at different depths. (a) The correlation between models and SEMUCB-WM1. The left panel shows the correlation coefficients at different depths and degrees. The right panel shows the total correlation r^{tot} for degrees 1–8 (solid curve) and degrees 1–20 (dashed curve). The total weighted correlation for degrees 1–8 (1–20) in a depth range of 50–2815 km is $<r_8> = 0.52$ ($<r_{20}> = 0.37$), while in the lower mantle is 0.55 (0.37). (b) Same as (a) except that the tomography is S40RTS. The total weighted correlation in a depth range of 50–2815 km is $<r_8> = 0.53$ and $<r_{20}> = 0.39$, while that in the lower mantle is $<r_8> = 0.56$ and $<r_{20}> = 0.38$.

0.51 and $<r_{20}> = 0.36$. From the distribution of correlation coefficient with depth and spherical harmonic degree, both Model 1 and Model 2 fit SEMUCB-WM1 and S40RTS well for shallow mantle and large-scale structures (Fig. 3). The correlation between model and tomography suggests that the models are consistent with tomography results in general (Fig. 3).

Of the two models considered, Model 1 behaves slightly better in the deep mantle (>1500 km) while Model 2 is better in the shallow mantle (<1500 km). Although Model 1 has larger total correlation coefficients (r_8^{tot} and r_{20}^{tot}) with tomography than Model 2, considering that Model 2 better predicts the geometry of individual slabs, especially that of Farallon and Nazca (Fig. 2), the main focus of this study, hereafter we will carry out a detailed analysis on slab migration based on Model 2.

4. Sinking rate of slabs

### 4.1. Temporal evolution of slabs in a global view

For an overall view of the temporally evolving slabs in the mantle, we first present the 3D distribution of slabs at different geological time (Fig. 4). At 120 Ma (80 Myr since the initial time), most slabs are shallow (<1000 km depth) and distributed near (<1500 km) their subduction zones. By 80 Ma, some slabs beneath East Asia, North America and near

the south pole are already in the deep (>2000 km depth) mantle while other slabs are still shallow (Fig. 4b). The lateral distance of the deepest slabs from trenches also significantly increases. During the Cenozoic (Fig. 4c,d), slabs along most subduction zones reached the deep mantle and eventually the CMB. The horizontal area these slabs cover steadily expands, with most deep slabs situated far away from their initial subduction locations. Parts of the northwestern slabs migrated for over 6000 km horizontally and lie beneath Europe at the present day.

This recorded temporal evolution of slabs in a global scale reveals that (1) slabs subducted at different locations could sink at different vertical rates, and (2) during a 200-Myr time frame, slabs can travel laterally for a continent-scale distance inside the mantle. These observations clearly contradict the vertical slab sinking trajectory at a constant rate commonly presumed in tomotectonic reconstructions. With this overview on slab evolution within the mantle, we subsequently perform more quantitative analyses on the slab sinking rate and its dependence on multiple subduction parameters, as presented in the following sections.

4.2. Depth distribution of modeled slabs versus subduction age and duration

For a quantitative calculation of the slab sinking rate, we first
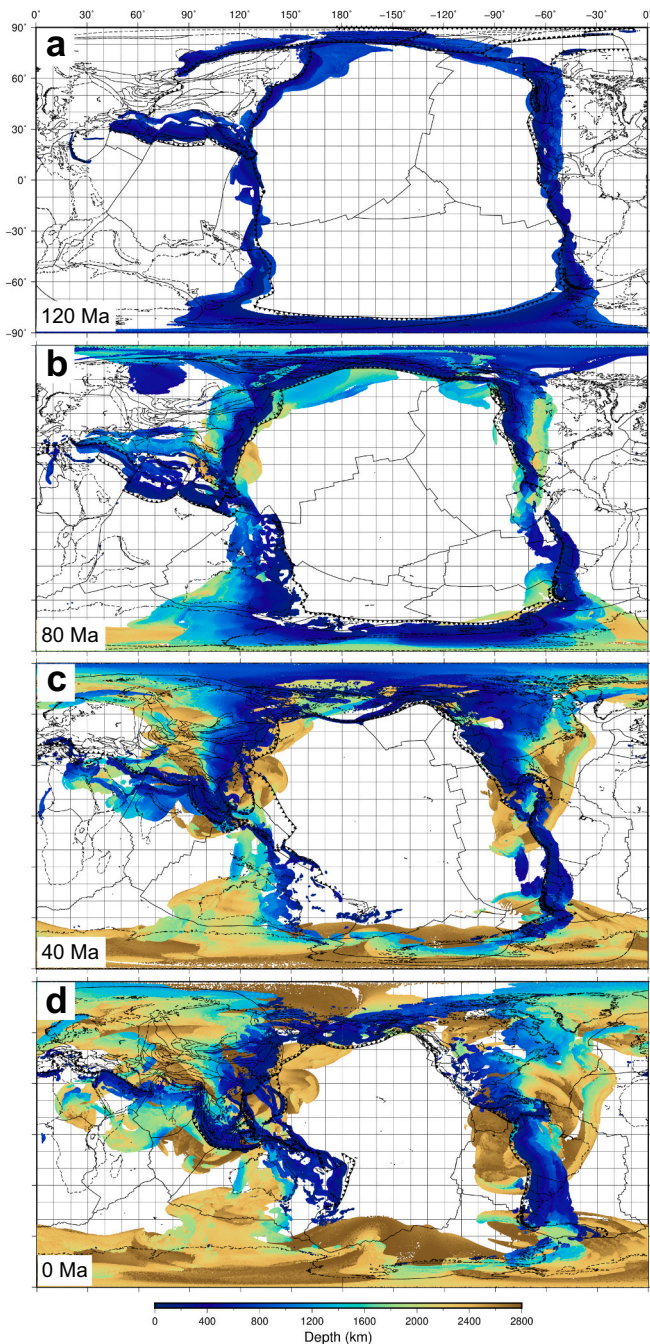
Fig. 4. The 4D evolution of subducted slabs since the Mesozoic. (a-d) Spatial distribution of cumulative slab geometry (represented by tracers at the interior of slabs) at 120 Ma, 80 Ma, 40 Ma and 0 Ma, respectively. The colour shows the depth of the slab.

examine the relationship between the present-day slab depth and the time it has spent inside the mantle (i.e., subduction duration). The depth of all slab tracers as a function of their subduction duration within the present mantle is shown in Fig. S2. While this plot is very informational, the high tracer density makes it difficult to illustrate the main trends of slab depth-age distribution.

To obtain a clearer relationship among this rich data set, we classify all data points into 199 groups, each corresponding to slabs subducted within a 1-Myr interval. The average depths and standard deviations for these slablets within the present-day mantle are calculated (Fig. 5). The slope of the resulting depth-age (i.e., subduction duration) curve

produces an apparent sinking rate of slabs.

A quick assessment of the result suggests that a constant 1.1 cm/yr slab sinking rate (the red line in Fig. 5a), as suggested by multiple previous tomotectonic reconstructions (Sigloch and Mihalynuk, 2013; van der Meer et al., 2010), clearly fails to describe the depth distribution of slab tracers. The linear trend based on this sinking rate connects the youngest (0 Ma) and oldest (200 Ma) slabs in the depth-age plot but misses most slabs in between.

Instead, a first order feature we observe from both the global plot (Fig. 5a) and that for individual subduction zones (Fig. 5b-f) is that the sinking rate of slabs is not uniform with depth or age. The globally averaged slab depth-age relationship (Fig. 5a) shows two kinks around 80 Ma and 130 Ma, respectively. Correspondingly, this requires three separate linear regressions for slabs subducted between 80 and 0 Ma, 120–90 Ma and prior to 130 Ma (formula presented in the Fig. 5). The large values of R^2 (the coefficient of determination) for 80–0 Ma and 120–90 Ma suggest that the slab depth is well proportional to subduction duration. Based on slabs subducted since 80 Ma, we obtain an apparent sinking rate of 2.1 cm/yr (sinking rates and the standard deviations are summarized in Table 1), while those subducted during 120–90 Ma suggests a reduced sinking rate of 1.4 cm/yr. These values are notably larger than previous estimates (e.g., Sigloch and Mihalynuk, 2013).

For the oldest slabs (>120 Ma), a linear regression leads to $R^2 = 0.59$, which dismisses a meaningful linear relation. In fact, these old slabs even show an opposite vertical motion to that of the younger slabs at greater depth. The reason is that, according to our models, after ~130 My since the initial subduction, majority of the slabs reached the lowermost mantle. The CMB, a nonpenetrative lower boundary of the mantle, prevents slabs from sinking further. As continuing subduction sends younger slabs from above, the older slabs lying on the CMB are pushed around and even forced to go upward. Thus, the oldest slabs demonstrate an overall negative sinking rate. The fact that most slabs reached the CMB after 130 My also suggests that the models starting from 200 Ma covers a long enough subduction history for measuring slab sinking rates. In addition, this implies that ancient mid-mantle slabs as old as 300 Ma adopted in previous studies (Sigloch and Mihalynuk, 2013; van der Meer et al., 2018; van der Meer et al., 2010) for estimating slab sinking rates are either much younger in age or represent ascending slabs from the CMB.

We also performed the same analysis for slabs subducted along major convergent boundaries, including northwestern Pacific, northeastern Pacific, southeastern Pacific, southwestern Pacific and Tethyan subduction zones. Some common features arise among these slabs that include (1) there is no linear depth-age relationship for slabs older than 120 Ma, which consistently suggest negative sinking rates, (2) the inferred sinking rate profiles along all subduction zones show a three-stage pattern.

Below the northwestern Pacific, the most recent turning point for slab sinking rate occurs around 55 Ma (Fig. 5b), where the rate after 50 Ma is 1.5 cm/yr, smaller than that during the preceding 120–60 Ma period. This reflects the effect of the Izanagi-Pacific mid-ocean ridge (MOR) subduction during the early Cenozoic. As revealed by Peng et al. (2021a), the MOR subduction led to the detachment of the Izanagi slab and formation of a regional westward mantle wind that caused the subsequent stagnation of the Pacific-Philippine Sea slabs at the base of the mantle transition zone. The Mesozoic Izanagi slab is generally older and has a larger cumulative volume than the Cenozoic slabs, causing the former to sink faster, while the significant lateral deflection of the latter following the mantle wind further reduces the Cenozoic slab sinking rate. For other subduction zones, the most recent turning point is around 80 Ma, same as the global average, which may reflect the effect of decelerating global plate motions during the Late Cretaceous (Müller et al., 2016).

There are also notable differences of slab sinking rates along the individual subduction zones. Among recently subducted slabs, the Farallon, Nazca and Tethyan slabs sink faster than the Pacific and Tonga
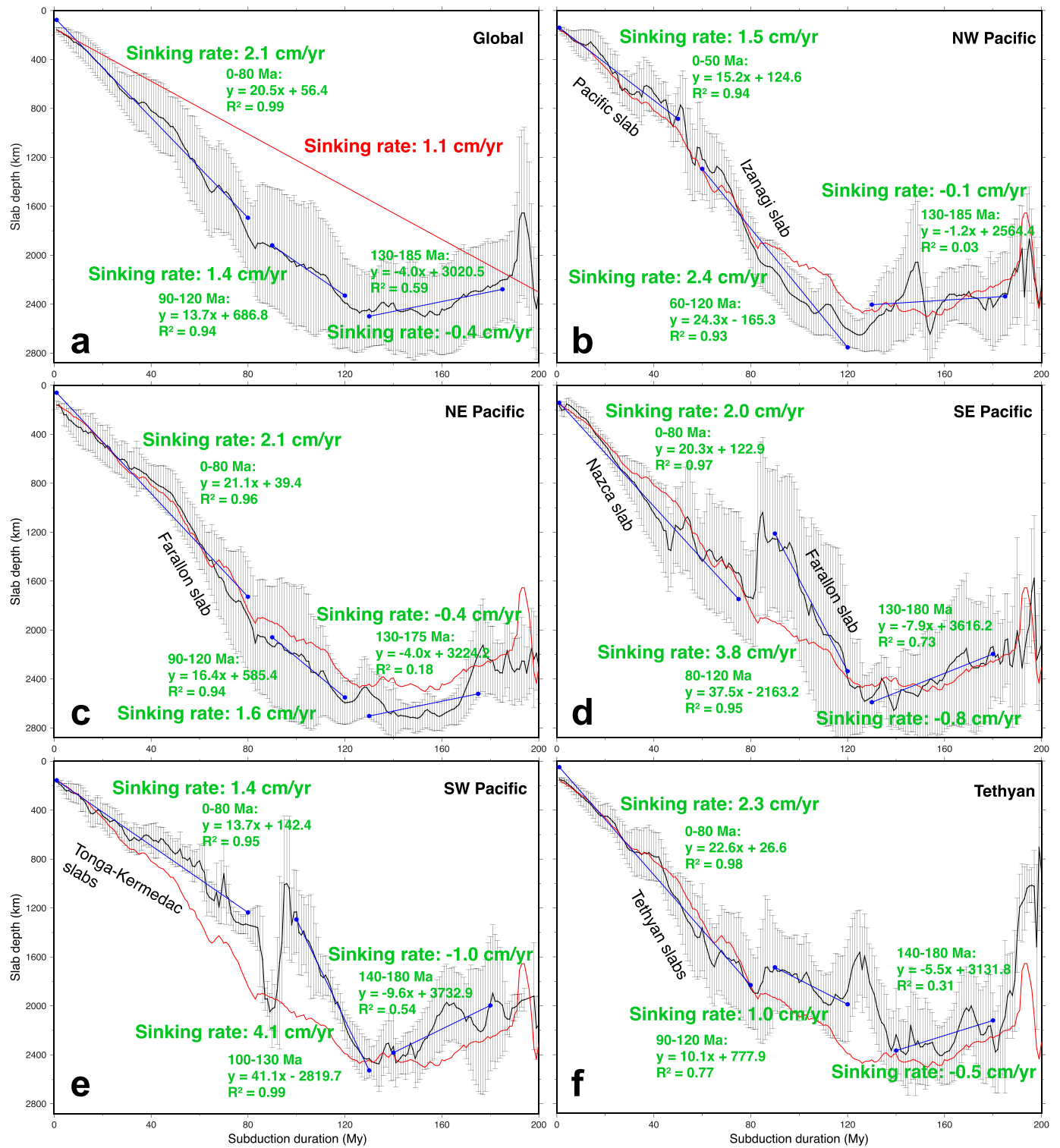
Fig. 5. Slab depth versus subduction duration within the present-day mantle. (a-c) The black curves show the averaged depth for slabs subducted at certain ages. The error bar shows one-sigma standard deviation in depth of the slablet with 1-Myr subduction duration. The results are for globally averaged slabs (a) or those subducted in northwestern Pacific (b), northeastern Pacific (c), southeastern Pacific, southwestern Pacific (e) and Tethyan subduction zone (f). The red curve in (b-f) shows the global average from a. The blue bars show the linear fits for data in certain age ranges (or subduction duration), with the formula and R^2 shown in black and sinking rates in blue. The straight red line in (a) has a constant sinking rate of 1.1 cm/yr. (For interpretation of the references to colour in this figure legend, the reader is referred to the web version of this article.)

Table 1
Sinking rates based on slab configuration of present day and of 80 Ma.

	Stage 1_present		Stage 2_present		Stage 1_80 Ma	
	SR[a]	Std dev[b]	SR	Std dev	SR	Std dev
Global	2.05	0.03	1.37	0.06	3.20	0.07
NW Pacific	1.52	0.05	2.43	0.09	3.84	0.06
NE Pacific	2.11	0.05	1.64	0.08	3.89	0.07
SE Pacific	2.03	0.04	3.75	0.15	3.28	0.09
SW Pacific	1.37	0.04	4.11	0.08	2.38	0.10
Tethyan	2.26	0.04	1.01	0.10	1.36	0.04

The 2nd and 3rd columns are for the first stage (0–80 Ma), with an exception of 0–50 Ma for NW Pacific, based on present-day slab configuration.
The 4th and 5th columns are for the second stage (90–120 Ma) with exceptions being 60–120 Ma for NW Pacific and 100–130 Ma for SW Pacific, based on present-day slab configuration.
The 6th and 7th columns are for the slabs subducted during the past 50 Myr based on slab configuration at 80 Ma.
[a] SR: sinking rate (cm/yr).
[b] Std dev: Standard deviation of sinking rate (cm/yr).

slabs. The slower sinking rates of the latter two seem to reflect the processes of slab stagnation at shallow mantle (660–1000 km) depths (Chang et al., 2016; Liu et al., 2021a; Ma et al., 2019; Mao and Zhong, 2018; Peng et al., 2021a). The sinking rate for slabs subducted from 120 Ma to 90 Ma (60 Ma for NW Pacific) varies more significantly (1.0–4.1 cm/yr) than that toward the present (1.4–2.3 cm/yr). We interpret this as reflecting the greater interference of the lowermost mantle on slab dynamics in the former. Consequently, the estimated slab sinking rate based on the present-day slab configuration demonstrates a strong dependence on both depth and geographic locations.

Besides the major properties of slab sinking rates demonstrated in Fig. 5, there is more information worth mentioning (Fig. S2). First, the depth-age distribution of present-day slabs is not always continuous, with some clear discontinuities where the amount of slab tracers is small. For the northwestern Pacific, there is a gap around 55 Ma (Fig. S2), which represents the mantle signature of the subducted Izanagi-Pacific MOR: the young oceanic plates abutting the 60-Ma MOR resisted subduction and created a subduction hiatus separating the Izanagi and Pacific slabs (Peng et al., 2021a). Similarly, there are several gaps within the southwestern Pacific slabs, also due to MOR subduction.

Second, for the recently subducted slabs, the standard deviations for the depth-age relationship are generally smaller (Fig. 5), because the slab tracers are more concentrated in space (Fig. S2). This suggests that the sinking rate derived with a linear regression is more reliable for the younger slab. For older (>120 Ma) slab, the tracers are more distributed, leading to larger standard deviations. Specifically, there are two groups of bifurcated slabs beneath eastern Pacific (Fig. S2c,d). One group shows continuous deepening with subduction age at mid-mantle depth below North America, representing the stagnant Farallon slabs around 1200 km (Fig. S2c). The other group is largely at the same depth below South America, representing the stagnant Nazca slab in the MTZ (Fig. S2d). These stagnant slabs are discussed in a recent review (Goes et al., 2017), and they generate much reduced slab sinking rates. Consequently, the large uncertainties in Fig. 5 for older slabs may be the reason why a global sinking rate is consistently smaller than that for individual slabs.

To further understand the possible time-dependence of slab sinking rate, as implied from the global turning point around 80 Ma of the depth-age slope (Fig. 5a), we then repeat this analysis based on the modeled slab configuration at 80 Ma (Fig. 6, Fig. S3). In this case, we observe a turning point at 50 Myr prior to 80 Ma (i.e., 130 Ma) for both the global average and individual subduction zones. In comparison, the globally averaged slab sinking rate during the recent 50 Myr prior to 80 Ma is 3.2 cm/yr (Fig. 6a), nearly 50% higher than that based on the present-day slab configuration (Fig. 5a). As shown later, this fast sinking rate is likely related to the overall fast plate motion and subduction rate during

the Cretaceous time. It implies that slab sinking rates inferred from the present-day slab configuration may not be applicable to the geological past.

Besides the overall faster slab sinking rates during the Cretaceous, there is also a greater geographic variation of the sinking rates relative to those inferred from the present-day slab configuration, where slabs subducted between 130 and 80 Ma beneath northwestern Pacific, northeastern Pacific and southeastern Pacific have notably larger sinking rate (3.3–3.9 cm/yr), but that beneath the Tethyan region is only 1.4 cm/yr (Fig. 6f), even slower than its Cenozoic sinking rate (Fig. 5f). These results further support the observation that slab sinking rate varies among subduction zones. These indicate that slab sinking rates are temporally and spatially variable.

4.3. Instantaneous slab sinking rates versus depth

The above linear regression based on the distribution of slab depth with subduction duration measures the average slab sinking rate over certain periods of time. The instantaneous sinking rate of slabs at different depths (Fig. 7) provides more information about slab dynamics and mantle properties. In this analysis, we exclude the slab that already reached the CMB which stopped sinking. As shown above, the slab sinking rate generally decreases toward the CMB (Figs. 5, 6), with the depth of 2300 km representing a common turning point where slab behaviors change from vertical sinking to flat lying. Therefore, as the depth of a slab tracer is greater than 2300 km, we define it as reaching the CMB and not include it in the calculation of the instantaneous slab sinking rate.

At 120 Ma (Fig. 7a), the instantaneous sinking rates below individual subduction zones strongly (>5-fold) vary, with the values ranging from <1 cm/yr to >5 cm/yr. Such differences diminish at all depths toward the present-day, when the lower-mantle sinking rates for different subduction zones are largely the same (Fig. 7d). We suggest that some fast sinking slabs prior to 80 Ma may partially reflect the largely vacant lower mantle at these times that posed less resistance to the incoming slabs (Fig. 4a), an effect that would decrease over time. However, this temporal effect should have little influence on geographic variation and depth dependence of slab sinking rates as discussed below (Fig. 5).

Consistent throughout most times are two depth ranges where the sinking rate locally peaks, with one above the MTZ (~300 km) and the other in the mid-mantle (~1000–1500 km). In contrast, the sinking rate toward the base of the MTZ marks a global minimum. The first peak is where slabs sink fast within the weak asthenosphere (Fig. S1). The trough at 500–700 km is likely due to the increased viscosity from the MTZ to the lower mantle and the buoyancy effect associated with the phase transformation at the 660 km discontinuity. Although at a reduced rate, slabs still sink continuously over depth, suggesting that these resisting forces are not enough to trap the slabs stagnant inside the MTZ (Peng et al., 2021a). The second peak in the lower mantle is more puzzling, as it is not associated with any major viscosity interface or phase transformation. We suggest this reflects the combined effect of slab acceleration after penetrating the resistant 660 km discontinuity, with the occurrence of slab avalanches below individual subduction zones, and the long-range braking effect of the reflective CMB from below.

The overall faster sinking rate in the upper mantle than that in lower mantle is consistent with their viscosity contrast, as commonly observed in previous studies (Bunge et al., 1998; Christensen, 1996; Liu and Stegman, 2011; Replumaz et al., 2004). The obvious effect of viscosity stratification on slab sinking rates is further illustrated in the comparison of slab depths in Model 1 and Model 2 (Fig. 8). Since Model 1 has smaller lower mantle viscosity than Model 2, the globally averaged sinking rate of slabs subducted in the recent 80 Ma are slightly faster in the former. As a corollary, the sinking rate of slabs may be applicable to inferring the viscosity properties of the convective mantle (Mao and Zhong, 2019; Peng et al., 2021a; van der Meer et al., 2018).
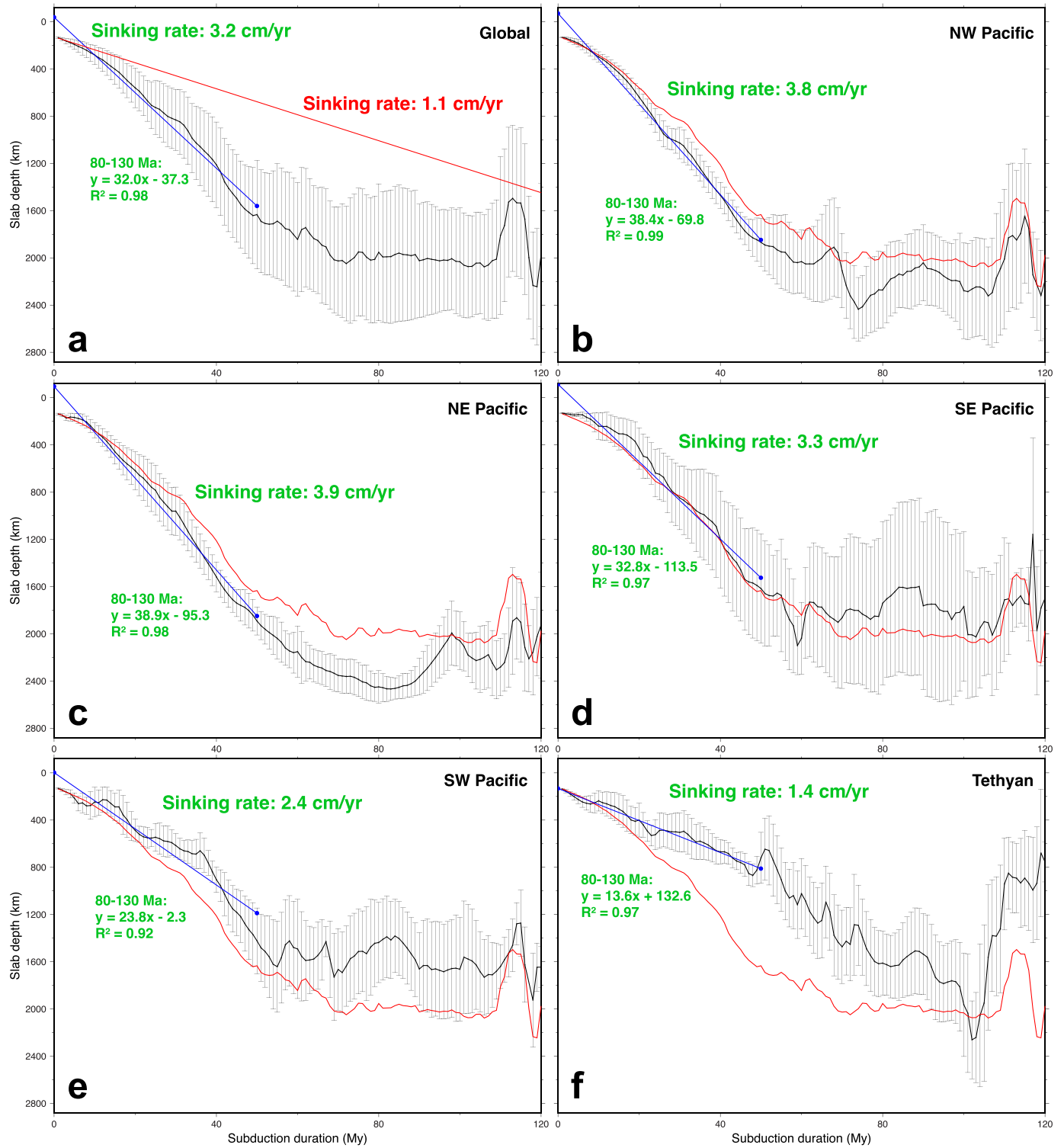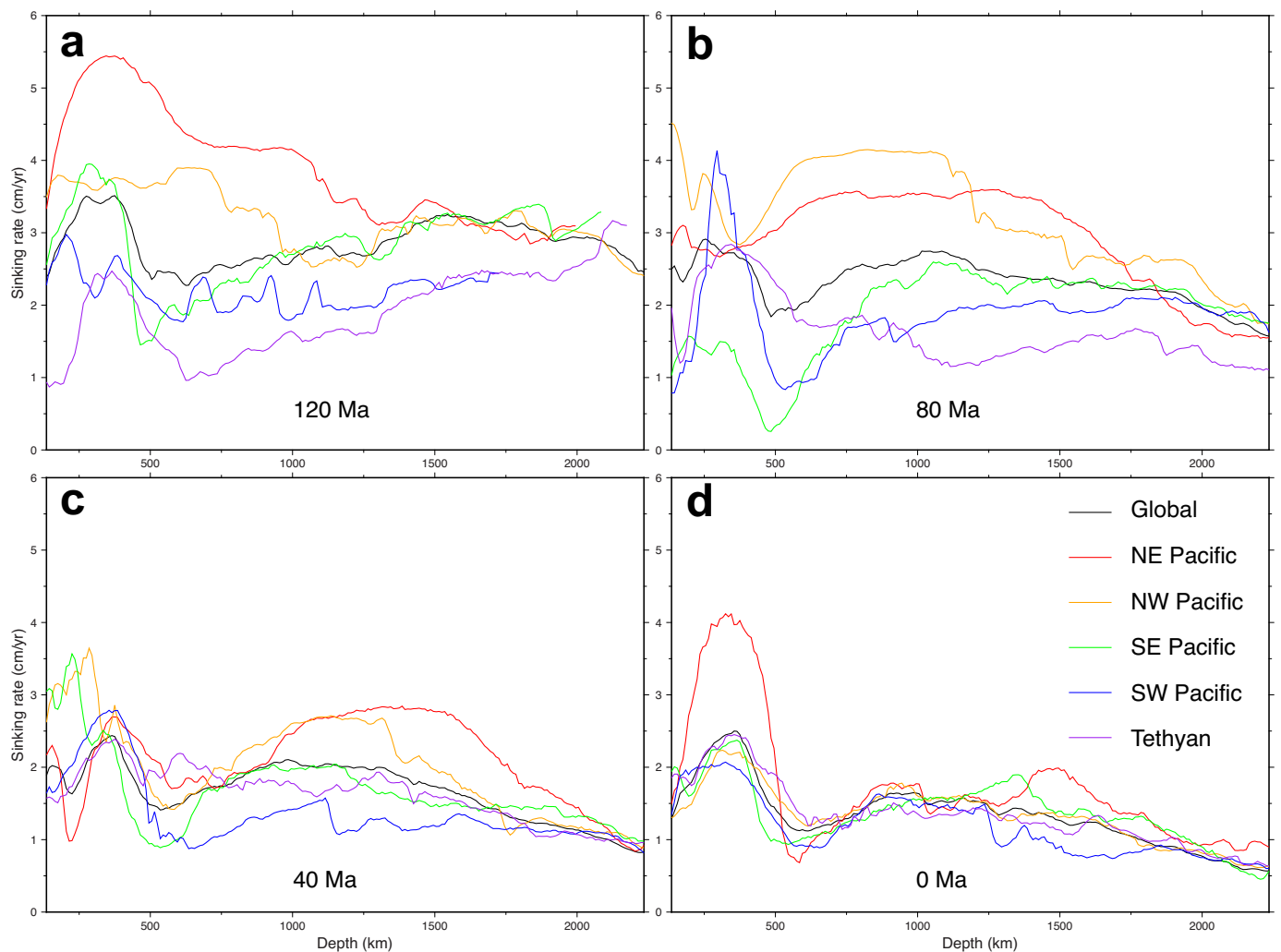
Fig. 6. Slab depth versus subduction duration at 80 Ma. All panels are the same as those in Fig. 5, but based on modeled slab configuration at 80 Ma (i.e. model runs from 200 Ma to 80 Ma).

Fig. 7. The distribution of slab sinking rate with slab depth. Each curve represents the averaged sinking rate of slab in a global scale or subducted at certain subduction zones. For each one, the average sinking rates at certain depths (with a 10-km range) are calculated. The slabs which reached the CMB are not counted.

4.4. Sinking rate versus subduction rate

Intuitively, the subduction rate of an oceanic plate and the slab dip angle determines the horizontal and vertical velocities of shallow slabs. This relationship, considering a long subduction history, may also extend into the lower mantle. Therefore, we further consider the effect of subduction rate on the slab sinking rate. We define the subduction rate as the average plate velocity along the trench, either globally or regionally (Fig. 9). Around 130 Ma, the subduction rate reached a global maximum, and the same is true for most individual subduction zones. Around 80 Ma, the globally averaged subduction rate had a secondary peak. These two turning points around 80 Ma and 130 Ma may be related to major plate reorganizations, when the global root mean square plate speeds reached the maximum values (Müller et al., 2019; Müller et al., 2016; Seton et al., 2012). Here, we compare this temporal pattern of plate motion since 200 Ma with both the horizontal and vertical components of slab motion, based on the present-day mantle configuration (Fig. 9).

The depth-averaged horizontal velocity of the subducting slabs is strongly correlated with the subduction rate, with their ups and downs closely following each other (Fig. 9). This is observed both at the global and regional scales (top row of Fig. 9), indicating a strong dynamic coupling of surface plate motion with that of the underlying mantle. Over increasing depth, the horizontal slab velocity generally decreases (middle row of Fig. 9). Within the upper mantle, this phenomenon is

expected because the major subducting plates that ultimately drive global plate motion (Forsyth and Uyeda, 1975) generate Couette-type flows with the amplitude of lateral velocities decreasing over depth (Hu et al., 2017; Peng et al., 2021a). Into the high-viscosity lower mantle, the further reduced horizontal velocity should reflect stronger viscous dissipation.

The temporal correlation between the subduction rate and depth-averaged sinking rate is much weaker (top row in Fig. 9), where most sub-50-Myr plate motion features are absent in the sinking rate. However, their long-term (>50 Myr) trends after 140 Ma generally correlate, suggesting that the global plate motion could influence the sinking rate by modulating the total volume of subducted slabs, and thus the buoyancy of mantle downwelling. This weak correlation is further demonstrated from the depth-distribution of slab sinking rates (lower row of Fig. 9), whose amplitude does not decrease with increasing depth as that of the horizontal velocities. Indeed, the depth variation of slab sinking rate (Fig. 7) is strongly influenced by the competition of slab buoyancy and mantle resistance at different depths, as analyzed above. Consequently, we show that the long-term (>50 Myr) subduction history influences slab sinking rates whose short-term (<50 Myr) variation mostly reflects the dynamic interaction of the sinking slab with the ambient mantle.
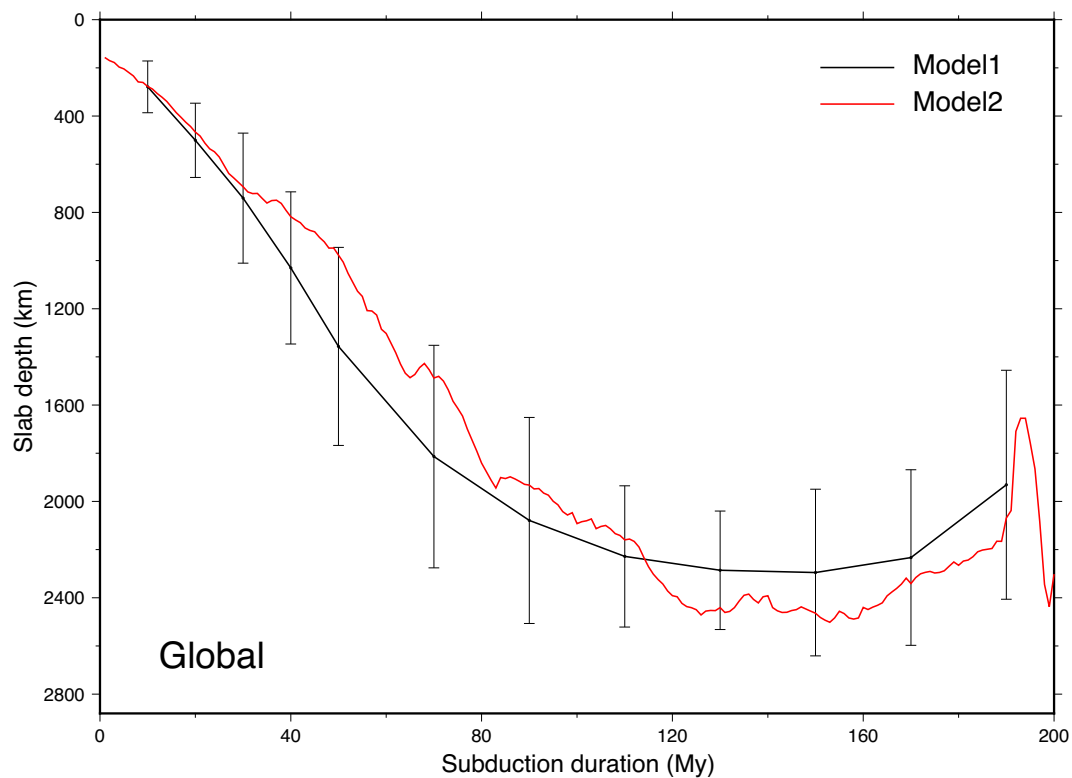
Fig. 8. The comparison between Model 1 (black curve with error bars) and Model 2 (red curve). For each model, the relationship between slab depth and subduction duration is calculated on a global scale at the present-day. (For interpretation of the references to colour in this figure legend, the reader is referred to the web version of this article.)

5. Discussion

In this study, we analyzed the migration of slabs in global subduction models that reproduce the present-day slabs in seismic tomography. We discussed both the lateral and vertical movement of slabs after subduction, with a focus on the latter. Besides the parameters discussed in Section 4, some other factors may also affect slab sinking rate, such as seafloor age and slab dip angle. The seafloor age controls the thermal structure, thus negative buoyancy, of oceanic lithosphere. However, the distribution of sinking rate with this factor does not show a clear dependence (Fig. S4). A possible reason is that subduction is a globally interacting process, where the buoyancy effect of a single slab is easily dwarfed by other factors. Indeed, the observation that the Cretaceous witnesses both younger seafloors (Fig. S4a,b) and fast slab sinking rates (Figs. 6, 7) confirms the minor role of slab buoyancy in controlling their sinking rate.

The slab dip angle, especially that measured over large depth ranges, represents another potential rate-affecting factor since it partitions the inferred horizontal and vertical velocities of a slab. Our models properly reproduce multiple present-day stagnant slabs including those below west Pacific, North America, and South America. These stagnant slabs all have smaller sinking rates than the more normal-dipping slabs (e.g., Fig. S2c,d). Albeit their local significance, these slabs with abnormal descending paths only occupy a small fraction of the total slab population at a given time (Figs. S2, 5), and thus do not notably change the average slab sinking rates. On the other hand, these flat-lying slabs represent extreme cases for the more commonly observed lateral motion of slabs, as discussed further below.

The obvious lateral motion of slabs poses a major challenge on the traditional wisdom of vertically sinking slabs inside the mantle. During the past 200 Ma, the modeled slabs can travel thousands of kilometers horizontally inside the mantle. The slabs beneath Europe observed by tomography may have originated from the northwestern Pacific (Fig. 4).

Similarly, a large portion of the subducted Tethyan slabs now lie beneath north Africa and the Indian Ocean (Fig. 4). Much of the Cretaceous Farallon slab subducted along the western coast of North America is now located beneath the southeast Pacific and mixed with the more recently (past 40 Ma) subducted Nazca slab (Fig. 4). This calls for caution in the exercise of locating the ancient trenches associated with the deep slabs beneath Europe, north Africa, Indian Ocean, and South America (Fig. 1a,d,g), since it is possible that these slabs may have originated from trenches far away at a different continent. For example, according to our models, the slabs now beneath eastern North America and the west Atlantic (Fig. 1a,d) represent the subducted Farallon slab along western North America, consistent with previous interpretations (Bunge and Grand, 2000; van der Meer et al., 2010). This inference, however, contrasts with the recent argument that these slabs record multiple Mesozoic intra-oceanic subduction events to the west of the North America (e.g., Sigloch and Mihalynuk, 2013). In addition, realizing the long-distance lateral slab migration could also reconcile the outstanding geologic debate on this problem (Pavlis et al., 2019), a topic that is beyond the scope of this study.

Another key finding from the above calculations is that almost all slabs sink through the mantle with spatially and temporally variable vertical rates. However, thus inferred slab sinking rates may need some deliberation as they are mostly based on a numerical model with sequential data assimilation, where the early part of the model evolution could be affected by the uncertain initial condition (Bunge et al., 1998; Liu and Gurnis, 2008). To minimize this impact, we avoid analyzing the slab properties during the first 80 Myr of model time. To make sure the post-120 Ma slab evolution (Figs. 4–7) is physically plausible, we further refer to some independent geologic constraints. As shown in a recent study (Peng et al., 2021b), the model predicts a regional-scale Late Cretaceous flat slab beneath East Asia (Fig. 4b), where the associated surface subsidence is consistent with the stratigraphic record of the Sichuan Basin and the continental-scale topographic inversion of East
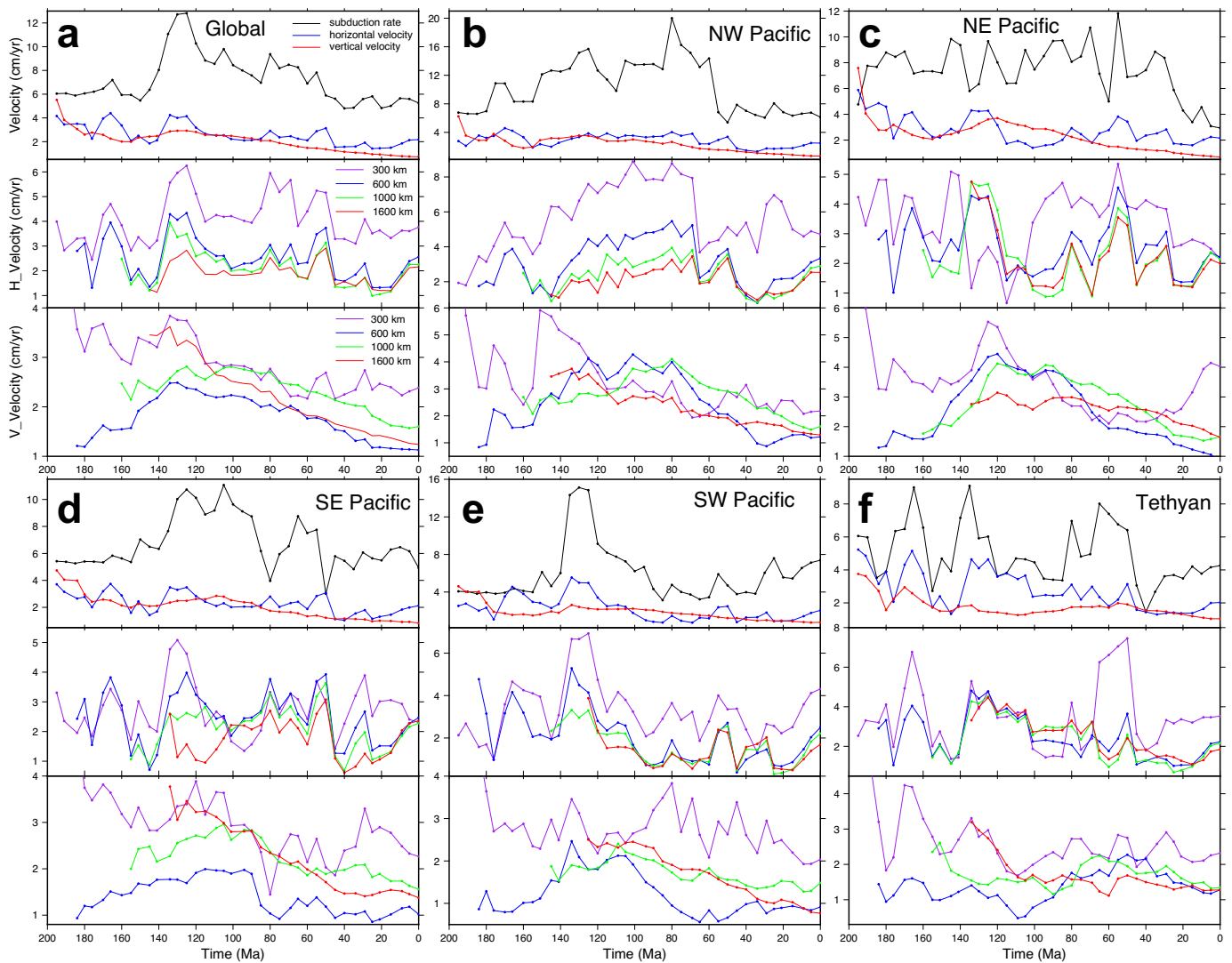
Fig. 9. Slab sinking rate versus depth as a function of time. In each of the 6 panels (a-f representing global and regional results), the horizontal axis is geological time, the vertical axes are velocities, with subduction rate being plate velocities near trenches, H_Velocity being horizontal velocity of slabs, and V_Verlocity being vertical velocity of slabs, i.e., sinking rate. In each panel, the upper row shows the subduction rate, depth-averaged horizontal slab velocity, and depth-averaged vertical slab velocity. The middle and lower rows show the region-averaged horizontal and vertical velocities for depths at 300, 600, 1000 and 1600 km, respectively.

Asia (Liu et al., 2021b), and the resulting lithospheric thinning also matches the seismic observation. The same global model also produces a Cretaceous flat Farallon slab (Fig. 4b), whose spatial and temporally extents are also similar to that inferred from an adjoint inverse model (Liu et al., 2008). Therefore, we conclude that the modeled slab evolution since at least the Early Cretaceous should be reasonable.

The slab sinking rates from this study are notably larger than most previous estimates based on tomography results (Butterworth et al., 2014; Clennett et al., 2020; Sigloch and Mihalynuk, 2013; van der Meer et al., 2018; van der Meer et al., 2010). Correspondingly, the associated trenches and geologic implications are younger than assumed in these studies. Mantle convection models generally suggest larger sinking rates (Butterworth et al., 2014; Shephard et al., 2012; Steinberger, 2000; Steinberger et al., 2012), among which the global average sinking rate in this study is the closest to that inferred by Steinberger et al. (2012). In addition, we find that a constant slab sinking rate does not exist, as the value changes dramatically among geographic locations and less so over geological time. A scenario close to that commonly adopted in recent tomotectonic reconstructions is when the slabs sink to the lower half (>1500 km) of the mantle but above the CMB, where a sinking rate of ~1 cm/yr is observed (Fig. 7d). However, such a scenario only exists

close to the present, as sinking rates during the past, especially the Mesozoic, are consistently above 2 cm/yr. We suggest that future estimates of subduction ages based on tomography should consider the variation of slab sinking rate with depth, time, and geographic location, as shown in Table 1 and Figs. 5–9.

6. Conclusion

Using global mantle convection models that properly reproduce the present slab geometry beneath major subduction zones, we quantitatively evaluate the issue of slab sinking rates. The main findings from this study include:

(1) Subducted slabs can migrate horizontally up to 6000 km, suggesting that the lateral location of observed slabs usually do not represent that of their paleo subduction zones.

(2) There does not exist a constant slab sinking rate, whose value varies with depth, subduction duration and geographic locations.

(3) Our inferred slab sinking rates are systematically higher than previously assumed, with that based on the past 80 Myr of

subduction ranging from 1.4 to 2.3 cm/yr and an average of 2.1 cm/yr.

(4) Future tomotectonic reconstructions should adopt more realistic slab sinking histories and revisit some geological constraints for past subduction.

CRediT authorship contribution statement

Diandian Peng: Conceptualization, Methodology, Software, Validation, Formal analysis, Investigation, Writing – original draft, Visualization. **Lijun Liu:** Supervision, Conceptualization, Validation, Writing – original draft, Funding acquisition.

Declaration of Competing Interest

The authors declare that they have no known competing financial interests or personal relationships that could have appeared to influence the work reported in this paper.

Acknowledgements

Appendix A. Supplementary data

Supplementary data to this article can be found online at https://doi.org/10.1016/j.earscirev.2022.104039.

References

Amaru, M.L., 2007. Global Travel Time Tomography with 3-D Reference Models. Geol. Traiectina, Utrecht Univ, pp. 1–174.

Becker, T.W., Boschi, L., 2002. A comparison of tomographic and geodynamic mantle models. Geochem. Geophys. Geosyst. 3, n/a–n/a. https://doi.org/10.1029/2001GC000168.

Bunge, H., Grand, S.P., 2000. Mesozoic plate-motion history below the Northeast Pacific Ocean from seismic images of the subducted Farallon slab. Nature 405, 337–340. https://doi.org/10.1038/35012586.

Bunge, H.-P., Richards, M.A., Lithgow-Bertelloni, C., Baumgardner, J.R., Grand, S.P., Romanowicz, B.A., 1998. Time scales and heterogeneous structure in geodynamic earth models. Science 280, 91–95. https://doi.org/10.1126/science.280.5360.91.

Butterworth, N.P., Talsma, A.S., Müller, R.D., Seton, M., Bunge, H.P., Schuberth, B.S.A., Shephard, G.E., Heine, C., 2014. Geological, tomographic, kinematic and geodynamic constraints on the dynamics of sinking slabs. J. Geodyn. 73, 1–13. https://doi.org/10.1016/j.jog.2013.10.006.

Chang, S.-J., Ferreira, A.M.G., Faccenda, M., 2016. Upper- and mid-mantle interaction between the Samoan plume and the Tonga–Kermadec slabs. Nat. Commun. 7, 10799. https://doi.org/10.1038/ncomms10799.

Christensen, U.R., 1996. The influence of trench migration on slab penetration into the lower mantle. Earth Planet. Sci. Lett. 140, 27–39. https://doi.org/10.1016/0012-821X(96)00023-4.

Clennett, E.J., Sigloch, K., Mihalynuk, M.G., Seton, M., Henderson, M.A., Hosseini, K., Mohammadzaheri, A., Johnston, S.T., Müller, R.D., 2020. A quantitative tomotectonic plate reconstruction of Western North America and the Eastern Pacific Basin. Geochem. Geophys. Geosyst. 21, 1–25. https://doi.org/10.1029/2020GC009117.

Domeier, M., Shephard, G.E., Jakob, J., Gaina, C., Doubrovine, P.V., Torsvik, T.H., 2017. Intraoceanic subduction spanned the Pacific in the Late Cretaceous–Paleocene. Sci. Adv. 3, 1–6. https://doi.org/10.1126/sciadv.aao2303.

Forsyth, D., Uyeda, S., 1975. On the relative importance of the driving forces of plate motion. Geophys. J. Int. 43, 163–200. https://doi.org/10.1111/j.1365-246X.1975.tb00631.x.

French, S.W., Romanowicz, B.A., 2014. Whole-mantle radially anisotropic shear velocity structure from spectral-element waveform tomography. Geophys. J. Int. 199, 1303–1327. https://doi.org/10.1093/gji/ggu334.

Fukao, Y., Obayashi, M., 2013. Subducted slabs stagnant above, penetrating through, and trapped below the 660 km discontinuity. J. Geophys. Res. Solid Earth 118, 5920–5938. https://doi.org/10.1002/2013JB010466.

Goes, S., Agrusta, R., van Hunen, J., Garel, F., 2017. Subduction-transition zone interaction: a review. Geosphere 13, 644–664. https://doi.org/10.1130/GES01476.1.

Grand, S.P., van der Hilst, R.D., Widiyantoro, S., 1997. Global seismic tomography: a snapshot of convection in the Earth. GSA Today 7, 1–7.

Hayes, G.P., Moore, G.L., Portner, D.E., Hearne, M., Flamme, H., Furtney, M., Smoczyk, G.M., 2018. Slab2, a comprehensive subduction zone geometry model. Science 362, 58–61. https://doi.org/10.1126/science.aat4723.

Hu, J., Faccenda, M., Liu, L., 2017. Subduction-controlled mantle flow and seismic anisotropy in South America. Earth Planet. Sci. Lett. 470, 13–24. https://doi.org/10.1016/j.epsl.2017.04.027.

Hu, J., Liu, L., Zhou, Q., 2018. Reproducing past subduction and mantle flow using high-resolution global convection models. Earth Planet. Phys. 2, 189–207. https://doi.org/10.26464/epp2018019.

Liu, L., 2014. Constraining cretaceous subduction polarity in eastern Pacific from seismic tomography and geodynamic modeling. Geophys. Res. Lett. 41, 8029–8036. https://doi.org/10.1002/2014GL061988.

Liu, L., Gurnis, M., 2008. Simultaneous inversion of mantle properties and initial conditions using an adjoint of mantle convection. J. Geophys. Res. Solid Earth 113, 1–17. https://doi.org/10.1029/2008JB005594.

Liu, L., Stegman, D.R., 2011. Segmentation of the Farallon slab. Earth Planet. Sci. Lett. 311, 1–10. https://doi.org/10.1016/j.epsl.2011.09.027.

Liu, L., Spasojević, S., Gurnis, M., 2008. Reconstructing farallon plate subduction beneath North America back to the late cretaceous. Science 322, 934–938. https://doi.org/10.1126/science.1162921.

Liu, S., Ma, P., Zhang, B., Gurnis, M., 2021a. The horizontal slab beneath East Asia and its subdued surface dynamic response. J. Geophys. Res. Solid Earth 126. https://doi.org/10.1029/2020JB021156.

Liu, L., Peng, D., Liu, Liang, Chen, L., Li, S., Wang, Y., Cao, Z., Feng, M., 2021b. East Asian lithosphere evolution dictated by multistage Mesozoic flat-slab subduction. Earth Sci. Rev. 217, 103621 https://doi.org/10.1016/j.earscirev.2021.103621.

Ma, P., Liu, S., Gurnis, M., Zhang, B., 2019. Slab horizontal subduction and slab tearing beneath East Asia. Geophys. Res. Lett. 46, 5161–5169. https://doi.org/10.1029/2018GL081703.

Mao, W., Zhong, S., 2018. Slab stagnation due to a reduced viscosity layer beneath the mantle transition zone. Nat. Geosci. 11, 876–881. https://doi.org/10.1038/s41561-018-0225-2.

Mao, W., Zhong, S., 2019. Controls on global mantle convective structures and their comparison with seismic models. J. Geophys. Res. Solid Earth 124, 9345–9372. https://doi.org/10.1029/2019JB017918.

McNamara, A.K., Zhong, S., 2004. Thermochemical structures within a spherical mantle: superplumes or piles? J. Geophys. Res. Solid Earth 109, 1–14. https://doi.org/10.1029/2003JB002847.

Müller, R.D., Seton, M., Zahirovic, S., Williams, S.E., Matthews, K.J., Wright, N.M., Shephard, G.E., Maloney, K.T., Barnett-Moore, N., Hosseinpour, M., Bower, D.J., Cannon, J., 2016. Ocean Basin evolution and global-scale plate reorganization events since Pangea breakup. Annu. Rev. Earth Planet. Sci. 44, 107–138. https://doi.org/10.1146/annurev-earth-060115-012211.

Müller, R.D., Zahirovic, S., Williams, S.E., Cannon, J., Seton, M., Bower, D.J., Tetley, M. G., Heine, C., Le Breton, E., Liu, S., Russell, S.H.J., Yang, T., Leonard, J., Gurnis, M., 2019. A global plate model including lithospheric deformation along major rifts and orogens since the triassic. Tectonics 38, 1884–1907. https://doi.org/10.1029/2018TC005462.

Pavlis, T.L., Amato, J.M., Trop, J.M., Ridgway, K.D., Roeske, S.M., Gehrels, G.E., 2019. Subduction polarity in ancient arcs: a call to integrate geology and geophysics to decipher the mesozoic tectonic history of the northern cordillera of North America. GSA Today 29, 4–10. https://doi.org/10.1130/GSATG402A.1.

Peng, D., Liu, L., Hu, J., Li, S., Liu, Y., 2021a. Formation of East Asian stagnant slabs due to a pressure-driven cenozoic mantle wind following mesozoic subduction. Geophys. Res. Lett. 48, 1–10. https://doi.org/10.1029/2021GL094638.

Peng, D., Liu, L., Wang, Y., 2021b. A newly discovered Late-cretaceous East Asian flat slab explains its unique lithospheric structure and tectonics. J. Geophys. Res. Solid Earth 126, 1–23. https://doi.org/10.1029/2021JB022103.

Replumaz, A., Kárason, H., van der Hilst, R.D., Besse, J., Tapponnier, P., 2004. 4-D evolution of SE Asia's mantle from geological reconstructions and seismic tomography. Earth Planet. Sci. Lett. 221, 103–115. https://doi.org/10.1016/S0012-821X(04)00070-6.

Replumaz, A., Negredo, A.M., Guillot, S., Villaseñor, A., 2010. Multiple episodes of continental subduction during India/Asia convergence: insight from seismic tomography and tectonic reconstruction. Tectonophysics 483, 125–134. https://doi.org/10.1016/j.tecto.2009.10.007.

Ritsema, J., Deuss, A., Van Heijst, H.J., Woodhouse, J.H., 2011. S40RTS: a degree-40 shear-velocity model for the mantle from new Rayleigh wave dispersion, teleseismic traveltime and normal-mode splitting function measurements. Geophys. J. Int. 184, 1223–1236. https://doi.org/10.1111/j.1365-246X.2010.04884.x.

Schellart, W.P., Kennett, B.L.N., Spakman, W., Amaru, M., 2009. Plate reconstructions and tomography reveal a fossil lower mantle slab below the Tasman Sea. Earth Planet. Sci. Lett. 278, 143–151. https://doi.org/10.1016/j.epsl.2008.11.004.

Seton, M., Müller, R.D., Zahirovic, S., Gaina, C., Torsvik, T., Shephard, G., Talsma, A., Gurnis, M., Turner, M., Maus, S., Chandler, M., 2012. Global continental and ocean

basin reconstructions since 200Ma. Earth Sci. Rev. 113, 212–270. https://doi.org/10.1016/j.earscirev.2012.03.002.

Sigloch, K., Mihalynuk, M.G., 2013. Intra-oceanic subduction shaped the assembly of Cordilleran North America. Nature 496, 50–56. https://doi.org/10.1038/nature12019.

Shephard, G.E., Bunge, H.P., Schuberth, B.S.A., Müller, R.D., Talsma, A.S., Moder, C., Landgrebe, T.C.W., 2012. Testing absolute plate reference frames and the implications for the generation of geodynamic mantle heterogeneity structure. Earth and Planetary Science Letters. https://doi.org/10.1016/j.epsl.2011.11.027, 317–318, 204–217.

Steinberger, B., 2000. Slabs in the lower mantle - results of dynamic modelling compared with tomographic images and the geoid. Physics of the Earth and Planetary Interiors 118, 241–257. https://doi.org/10.1016/S0031-9201(99)00172-7.

Steinberger, B., Torsvik, T.H., Becker, T.W., 2012. Subduction to the lower mantle - A comparison between geodynamic and tomographic models. Solid Earth 3, 415–432. https://doi.org/10.5194/se-3-415-2012.

Tan, E., Choi, E., Thoutireddy, P., Gurnis, M., Aivazis, M., 2006. GeoFramework: coupling multiple models of mantle convection within a computational framework. Geochem. Geophys. Geosyst. 7, 1–14. https://doi.org/10.1029/2005GC001155.

van der Meer, D.G., Spakman, W., van Hinsbergen, D.J.J., Amaru, M.L., Torsvik, T.H., 2010. Towards absolute plate motions constrained by lower-mantle slab remnants. Nat. Geosci. 3, 36–40. https://doi.org/10.1038/ngeo708.

van der Meer, D.G., van Hinsbergen, D.J.J., Spakman, W., 2018. Atlas of the underworld: slab remnants in the mantle, their sinking history, and a new outlook on lower mantle viscosity. Tectonophysics 723, 309–448. https://doi.org/10.1016/j.tecto.2017.10.004.

Wu, J., Suppe, J., 2018. Proto-South China sea plate tectonics using subducted slab constraints from tomography. J. Earth Sci. 29, 1304–1318. https://doi.org/10.1007/s12583-017-0813-x.

Wu, J., Suppe, J., Lu, R., Kanda, R., 2016. Philippine Sea and East Asian plate tectonics since 52 Ma constrained by new subducted slab reconstruction methods. J. Geophys. Res. Solid Earth 121, 4670–4741. https://doi.org/10.1002/2016JB012923.

Zhong, S., McNamara, A., Tan, E., Moresi, L., Gurnis, M., 2008. A benchmark study on mantle convection in a 3-D spherical shell using CitcomS. Geochem. Geophys. Geosyst. 9, 1–32. https://doi.org/10.1029/2008GC002048.